

Spatial and Pulse Efficiency Constraints in Atom Interferometric Gravitational Wave Detectors

P Schach  and E Giese ¹

¹ *Technische Universität Darmstadt, Fachbereich Physik, Institut für Angewandte Physik, Schlossgartenstr. 7, 64289 Darmstadt, Germany*

Currently planned and constructed terrestrial detectors for gravitational waves and dark matter based on differential light-pulse atom interferometry are designed around three primary strategies to enhance their sensitivity: (i) Resonant-mode enhancement using multiple diamonds, (ii) large-momentum-transfer techniques to increase arm separation within the interferometer, and (iii) very-long baseline schemes that increase the distance between the two interferometers. Both resonant-mode enhancement and large-momentum-transfer techniques result in a greater number of light pulses, making high pulse fidelity during atom-light interactions imperative. At the same time, increasing the number of diamonds in vertical configurations leads to taller atomic fountains, which consequently reduces the available distance between interferometers. As a result, the number of diamonds, large-momentum-transfer pulses, and the fountain height are interdependent parameters that must be carefully balanced. In this work, we present optimal configurations for multi-diamond geometries, explicitly accounting for the spatial extent of a single interferometer, considering constraints imposed by the baseline dimensions and atomic losses due to imperfect pulses. We provide practical analytical relations to estimate the optimal number of pulses that should be applied. Many proposals beyond demonstrator experiments require pulse numbers that demand efficiencies not yet demonstrated with state-of-the-art momentum transfer techniques. As a result, the observed sensitivity falls short of expectations—an effect caused by both arm separation and atom loss per pulse—highlighting the urgent need for research aimed at improving pulse fidelities.

I. INTRODUCTION

Terrestrial very-long baseline atom interferometers [1–3] for the detection of gravitational waves [4–7] and dark-matter candidates [8–10] are currently planned or under construction, *i. e.*, the MAGIS [11], AION [12], ELGAR [13], ZAIGA [14], and MIGA [15] initiatives. These instruments are designed to complement traditional optical interferometers by filling the sensitivity gap in the frequency range from 0.01 Hz to a few Hertz. To suppress common-mode noise, the proposals employ differential measurements between two spatially-separated interferometers, which are aligned either vertically or horizontally. Other noise sources such as Newtonian or gravity-gradient noise [16–20] pose significant challenges for gravitational-wave detection in the low-frequency band of the targeted regime. However, correlation methods [21, 22] offer an approach to reduce the impact of these noise sources. Differential laser phase noise [23, 24] can be effectively suppressed by employing single-photon transitions [25–28], while other setups relying on cavity-based two-photon transitions [15] must develop special techniques to address this challenge.

In principle, three primary strategies can be employed to enhance the sensitivity of the detectors. The first involves increasing the number of atom–light interaction points by implementing large-momentum-transfer (LMT) methods. The most prominent LMT techniques include Bloch oscillations [29–33], double diffraction [34–36], higher-order diffraction [37, 38], and the application of sequential pulses [27, 39, 40], which are most commonly employed with single-photon transitions and which will be the focus of our discussion below. The second method

relies on resonant-mode amplification [7] and is implemented by matching the frequency of the gravitational wave to the interrogation time of a single loop of a multi-diamond configuration [41–45]. As a result, the signal amplitude scales with the number of diamonds. While in some configurations the roles of the interferometer arms are interchanged with each diamond, the majority of proposed schemes introduce a mirror pulse after each diamond, thereby preventing arm crossings and allowing the phase difference to accumulate coherently. This latter scheme is the focus of the present article. The third strategy improves sensitivity by using very large baselines, as this increases the difference between two local interferometers that interact with the gravitational wave at different points in space and time. However, this approach is limited by spatial constraints, particularly for terrestrial and vertical configurations, where the interferometer arms may eventually reach the top or bottom of the available baseline. In contrast, for horizontal configurations, neither the interferometer duration nor the fountain height directly reduces the available baseline length. However, these parameters cannot be increased indefinitely as they are limited by the transverse dimensions of the detector and may have to resort to relaunch strategies [46, 47]. All of these strategies are interdependent and must be carefully balanced to optimize overall detector performance, as we discuss in this article.

The total number of applied diffraction pulses is determined by the number of pulses per LMT sequence and diamonds, which in turn is related to the number of applied beam splitter or mirror sequences. As a general rule, a larger total number of pulses is typically desired. However, the total number of pulses is significantly con-

strained by the pulse fidelity, as imperfections in each pulse reduce the number of detected atoms, ultimately degrading the sensitivity due to shot noise. Hence, there must be a trade-off between signal enhancement achieved by increasing the number of LMT pulses or diamonds and the increase in shot noise caused by atom loss. Previous work [48] optimizes the fountain height for a given baseline, a fixed number of diamonds, and a specific number of LMT pulses. In these studies, the number of diamonds and the number of LMT pulses were treated as independent, predetermined parameters, and the difference in arm lengths within the interferometer was not explicitly considered.

Imperfect fidelities limit the total number of pulses that can be distributed between diamonds and LMT pulses. Simultaneously, operating a large number of diamonds in resonant mode increases the required fountain height, while employing a greater number of LMT pulses leads to larger arm separations within the interferometer. Both effects result in the interferometer occupying greater fractions of the available baseline. In contrast to terrestrial atom interferometers, these spatial constraints do not necessarily apply to space-based [49] or vertical proposals [13, 15]. For example, in the MAGIS-space proposal [7], optimization parameters are constrained by the maximal number of pulses and the maximal interferometer duration, but there are no spatial restrictions imposed by the baseline, as the atom interferometers are placed on separate satellites.

In this article, we determine optimal configurations for differential geometries based on experimentally available parameters. Previous optimizations have not explicitly accounted for the effects of arm separation within a single interferometer or imperfect pulse efficiency. We explicitly incorporate spatial limitations introduced by the baseline for the fountain height and arm separation, as well as losses per pulse in the optimization process. In contrast to previous approaches [48], we assume that the atom flux of the source is independent of the interferometer duration, implying an interleaved operation [50] if necessary.

After defining the considered configuration in section II, we optimize for the fountain height and total number of pulses for which the explicit derivation is outlined in appendix A. Other quantities such as the number of diamonds and number of LMT pulses are derived from these optimized parameters. In section III, we establish concise analytical relations to estimate the optimal number of pulses within an experiment as a function of key experimental parameters. To leading order, we observe that the optimal pulse number is determined solely by atomic losses per pulse. Moreover, we derive analytical conditions to identify the parameter space where the arm separation becomes relevant. Finally, in section III we incorporate the spatial constraints into a numerical optimization and compare the results to the analytical approach that neglects restrictions. We find that most proposals beyond demonstration experiments require pulse numbers that imply efficiencies that have not yet been demonstrated

with state-of-the-art LMT techniques, highlighting the urgent need for research aimed at enhancing pulse fidelities. We summarize our results and establish their connection to previous studies in section VI.

II. SETUP

In this article, we consider a differential configuration to measure phase fluctuations induced by a gravitational wave between two vertically-aligned Mach-Zehnder interferometers. In such a differential geometry, common-mode phase-noise contributions are reduced. To suppress remaining laser phase fluctuations, the beam-splitter and mirror pulses in each interferometer are realized by single-photon transitions [25–28] with laser wave vector k that corresponds to an optical wavelength. The two interferometers are separated by a distance L and confined within the baseline B , which represents the ultimate spatial resource in such very-large baseline setups, see figure 1. In addition, the baseline limits the other relevant spatial quantities, namely the maximum allowable arm separation and spatial extent or fountain height of the interferometers, fundamentally constraining the interferometer design and sensitivity. For large baselines, the finite speed of light c introduces significant time delays $\tau_L = L/c$ between both interferometers and $\tau_B = B/c$ along the whole baseline. Effects due to finite speed of light over the extent of a single interferometer with fountain height $H = B - L$ are neglected in the following.

Utilizing the full capabilities of differential Mach-Zehnder interferometers, two modes of operation are possible: (i) in resonant mode [7] the interferometer time T is matched to the frequency of a gravitational wave $f = \omega/(2\pi)$ through the condition $\omega T = \pi$, (ii) while in broadband mode [51] this condition is relaxed, allowing the interferometer to respond over a wider frequency range at the cost of reduced peak sensitivity. To further amplify the gravitational wave signal, we allow for a multi-diamond scheme characterized by the number of diamonds Q . This configuration increases the signal amplitude, effectively providing a Q -fold resonant enhancement. However, this increased sensitivity comes with narrower resonances, reducing the bandwidth of the detector and making it more selective to specific frequencies.

Instead of applying a single light pulse for each beam-splitter and mirror, LMT techniques can be incorporated to significantly increase the spatial separation between the two arms within each diamond. Specifically, each beam splitter and mirror now consists of a sequence of N pulses, resulting in an increase in the transferred momentum by the factor N . Figure 1(a) visualizes the differential multi-diamond scheme for many diamonds (left) and a single diamond (right).

The signal amplitude [7] of the differential phase between both interferometers for a gravitational wave of strain h in the low-frequency band for $\omega\tau_B \ll 1$ and

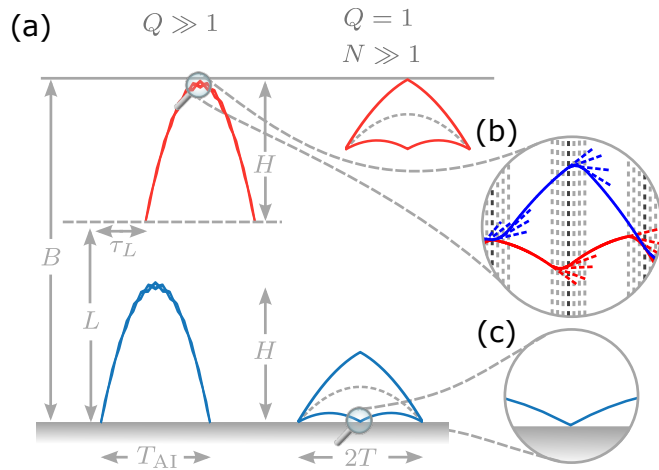


Figure 1. (a) Differential configuration of two atomic Mach-Zehnder interferometers, each with a fountain height H , separated by a distance L and confined within a baseline of length B . Each interferometer consists of Q diamonds, leading to a total interferometer time $T_{\text{AI}} = 2QT$ for an interrogation time T . The LMT beam splitters and mirrors are implemented via a sequence of N single-photon pulses, see inset (b). The finite speed of light introduces a time delay τ_L between the lower and upper interferometer. The left panel illustrates the case of many diamonds, while the right panel depicts a single diamond. (b) Visualization of the parasitic paths and atom losses that emerge from imperfect LMT pulses within a single diamond. The vertical extent of both interferometers is ultimately constrained by the bottom and top of the available baseline, so the atoms are ideally reflected before they hit the ground (c).

resonant mode $\omega T = \pi$ is given by

$$\Phi = 2hkLNQ |\text{sinc}(\omega\tau_B N)| \quad (1)$$

and is obtained by averaging the second moment of the differential phase over uniformly distributed phases of the gravitational wave [8]. For typical frequencies around [52] 1 Hz and a baseline of [11] 100 m, the low-frequency approximation is well satisfied $\omega\tau_B \sim 10^{-6} \ll 1$. Assuming additionally a moderate number of pulses such that the condition $\omega\tau_B N \ll 1$ holds, the signal amplitude simplifies to

$$\Phi \approx 2hkLNQ. \quad (2)$$

The corresponding strain sensitivity parametrized by the uncertainty

$$\Delta h = \frac{\Delta\Phi}{2kLNQ} \quad (3)$$

is readily derived from Gaussian error propagation.

We assume that the uncertainty $\Delta\Phi$ of the signal amplitude is shot-noise limited or at least scales like shot noise with the number of atoms. Moreover, we consider that phase uncertainties arising from both external factors and technical noise sources can be efficiently mitigated. The same reasoning is applied to Newtonian or gravity-gradient noise which limits sensitivity in the low-frequency band [16, 18, 53], for example by relying on mitigation strategies like correlation methods [21]. Under these assumptions, the phase uncertainty becomes $\Delta\Phi = \sqrt{2/(\nu N_{\text{at}})}$ with the number of detected atoms

N_{at} and number of repetitions ν . We observe that the strain uncertainty in equation (3) scales with the number of LMT pulses, which in turn contributes to the total number of applied light pulses N_P . In experimental implementations, imperfect pulse efficiency induces atom loss, reducing the number of detected atoms according to $N_{\text{at}} = N_0(1 - \lambda)^{N_P}$, where λ is the loss per shot. Simultaneously, pulse imperfections may generate parasitic paths, as sketched in figure 1(b). These unwanted paths can couple into the interferometer output port and fundamentally modify the interferometric response, an effect that we neglect here but that underlines the importance of mitigating such issues [54–58]. Incorporating atom losses, the strain uncertainty takes the form

$$\Delta h = \frac{\Delta\Phi(\lambda)}{2kLNQ} = \sqrt{\frac{2}{\nu N_0(1 - \lambda)^{N_P}}} \frac{1}{2kLNQ} \quad (4)$$

with the initial number of atoms N_0 and relative losses per pulse λ . In the following, we restrict our discussion to atom loss and exclude other mechanisms that may lead to decoherence or a reduction in contrast, specifically omitting the effects of parasitic path coupling into the exit port [59–62]. Here we observe a trade-off between two effects: (i) atom losses increase the phase uncertainty by reducing the number of detected atoms, while (ii) a greater number of pulses per LMT sequence or more diamonds amplify the signal. Previous optimization approaches did not account for this trade-off and typically assumed a fixed maximal number of pulses [48]. In contrast, we derive conditions incorporating both effects and identify optimal configurations.

III. ANALYTICAL OPTIMIZATION

Based on the strain uncertainty from equation (4), we are able to identify optimal configurations for a given pulse efficiency. To obtain analytical relations, we make two assumptions, which we will relax later. First, we connect the total interferometer duration $T_{\text{AI}} = 2QT$ to the fountain time $T_{\text{tot}} = \sqrt{8H/g}$ of a fountain in a vertical setup. Similarly to previous studies [48], we assume $T_{\text{AI}} = T_{\text{tot}}$, which leads to $Q = \xi\sqrt{\ell}$ with a scaling factor $\xi = \sqrt{2B/(gT^2)}$ and the relative height $\ell = H/B$. Because interleaved operation [50] is possible, we assume a fixed number of repetitions, so that the number of experimental repetitions ν is independent of the total interferometer time T_{AI} and the interrogation time T . The total number of pulses N_P is a key parameter for the sensitivity and is related to the number of diamonds and LMT pulses by the relation $N_P = 4QN - 2Q + 1$. This assumption differs from previous treatments [48], in which Q and N were treated as independent quantities and the repetition rate was determined by the interferometer duration. In addition, we assume lower bounds for the number of diamonds $Q \geq 1$ and LMT pulses $N \geq 2$. The latter condition reflects the fact that between two pulse sequences both interferometer arms are in the ground state to avoid spontaneous emission or noise arising from populating different internal states. Taking into account both assumptions, we optimize the sensitivity from equation (4) with respect to the relative height ℓ and the total number of pulses N_P . The analytical relations for the optimal number of pulses N_P and relative height ℓ are provided in appendix A1. Based on these relations, the quantities Q and N are not necessarily integers. Although the non-integer character of the number of diamonds and LMT pulses is not physical, the analytical relations for the optimal parameters nonetheless provide valuable insights into the optimization process. In section V, we perform a numerical optimization with Q and N restricted to integer values and compare the results to the analytical observations.

The relation for the optimal number of pulses and its distribution between the number of diamonds and pulses per LMT sequence are plotted in figure 2(a). We observe that a lower pulse efficiency (increased loss λ) leads to a reduced total number of pulses, which for low frequencies appears to be independent of both the baseline and the frequency. Hence, in the low-frequency band of the targeted regime, the optimal number of pulses is primarily limited by the pulse efficiency.

For small losses per pulse $\lambda \ll 1$, the total number of pulses in equation (A4) is approximated by

$$N_P \approx \frac{2}{\lambda} + \left(-\frac{1}{6} - \xi^2\right) \lambda. \quad (5)$$

As expected, the pulse number is limited by the relative losses per pulse. In particular, the approximation provides an estimate of the optimal number of pulses for given

pulse efficiencies. Conversely, for a specified number of pulses, the required pulse efficiency can be estimated to optimally utilize the available pulses. The approximation consists of two terms: (i) the first, dominant term is independent of both baseline and frequency and inversely proportional to λ , while (ii) the second term scales linearly with λ , depends on baseline and frequency, and can become significant under certain conditions.

The total number of pulses, set by the pulse efficiency, can be allocated between increasing the number of LMT pulses (which results in greater arm separation) and the number of diamonds. Since the sensitivity scales with the distance $L/B = (1 - \ell)$ between both interferometers and the number of diamonds Q , small fountain heights and large numbers of diamonds are desired. However, the fountain height is connected to the number of diamonds by $Q \sim f\sqrt{\ell}$, leading to a trade-off between fountain height and number of diamonds. Nevertheless, higher frequencies lead to shorter interrogation times $T = 1/(2f)$ in resonant mode, and consequently result in a greater number of diamonds for the same interferometer height. Hence, we observe an increased number of diamonds for larger frequencies in the analytical optimization, visualized in figure 2(a). While at low frequencies the number of diamonds is limited by a single diamond, at high frequencies there exists an upper bound for the optimal number of diamonds due to the constraint $N \geq 2$ and the relationship between the number of diamonds and LMT pulses through the total number of pulses. The optimal pulse number is primarily determined by the pulse efficiency.

IV. ROLE OF ARM SEPARATION

So far, we have neglected the arm separation for each interferometer, which becomes increasingly relevant when considering the large number of LMT pulses proposed in recent schemes [11, 12]. To check whether the trajectories implied by the analytical optimization for different pulse efficiencies and frequencies are confined within the baseline, we define the arm separation $\Delta z = N\hbar kT/m$ with the atomic mass m and the maximal height of a fountain $H = \ell B + \Delta z/2$. Two scenarios can occur: the atom interferometer reaches (i) the ceiling or (ii) the bottom of the baseline. To obtain an analytical condition for the first scenario, we assume low frequencies where a single diamond is optimal. Starting from the relation $Q = \xi\sqrt{\ell} = 1$, we find

$$\ell = \frac{g}{8B} \frac{1}{f^2} < 1, \quad (6)$$

which sets a lower limit on the frequency resolvable in resonant mode by a given baseline, visualized by the blue shaded regions in figure 2(b). In the second scenario, the arm separation exceeds the fountain height $H/\Delta z > 1$, causing the lower interferometer arm to hit the bottom of the baseline, as visualized in figure 1(c). Using equations (A4), (A5), and (A6), we identify the parameter

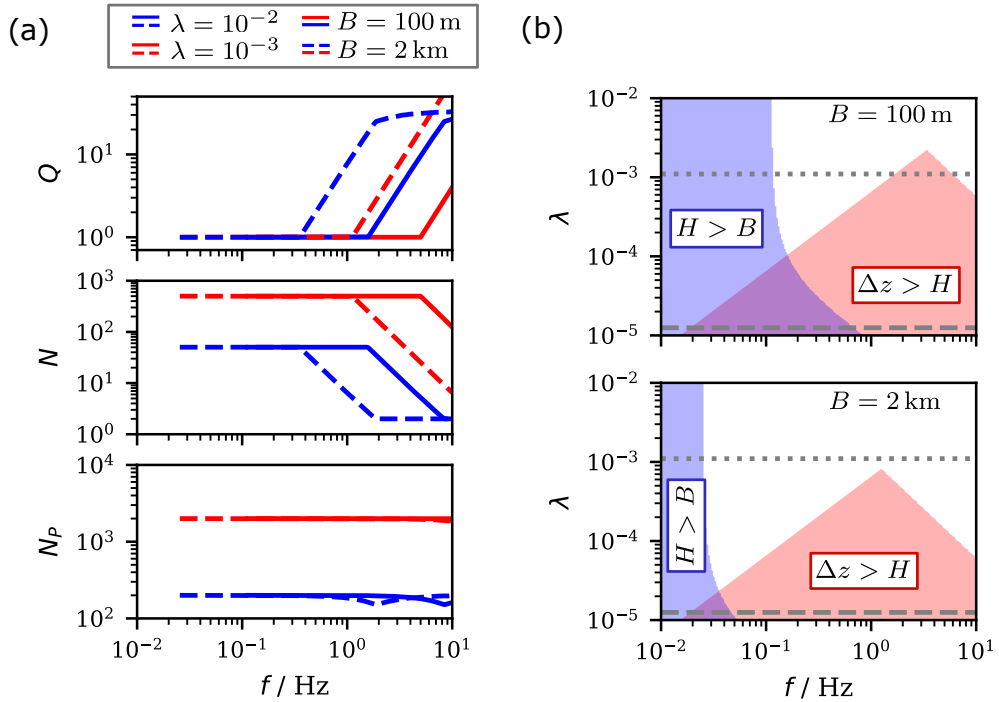


Figure 2. (a) Distribution of the optimal number of pulses N_P between the number of diamonds Q and LMT pulses N , as a function of the gravitational wave frequency f , shown for two different losses per pulse λ (red and blue) and baselines B (solid and dashed). Assuming the entire fountain height can be exploited in an experiment and the arm separation can be neglected, we optimized the sensitivity from equation (4) with respect to the relative fountain height $\ell = H/B$ and the total number of pulses N_P . (b) Taking into account the arm separation Δz within a single interferometer, we find parameter spaces where the atomic cloud reaches the bottom (red shaded region) or top (blue shaded region) of the available baseline, and a numerical treatment becomes necessary.

space where the interferometer is constrained by the bottom of the baseline. In the limit $\lambda \ll 1$ and in the regime where a single diamond is optimal, the parameter space is restricted by $\lambda > f/\eta$ with $\eta = gm/(\hbar k)$. In contrast, for $Q > 1$ and $N > 2$ the condition has the form

$$\lambda > \left[\frac{8}{\eta} \left(\frac{g}{8B} \right)^3 f^{-5} \right]^{\frac{1}{4}}. \quad (7)$$

Both cases are visualized by the red shaded triangles in figure 2(b).

We observe that for the baseline $B = 100$ m, the arm separation becomes relevant at lower pulse efficiencies and higher frequencies compared to the larger baseline $B = 2$ km, consistent with the condition given in equation (7). Current proposals [11] assume a large number of pulses per LMT sequence with $N = 4 \times 10^4$, resulting in a total number of pulses of approximately $N_P \approx 1.6 \times 10^5$ for a single diamond. Consulting equation (5) to optimally utilize the large number of pulses proposed, a loss of approximately $\lambda \approx 1.25 \times 10^{-5}$ per pulse is required. The required efficiency is indicated by the dashed line in figure 2(b), which overlaps completely with the shaded regions corresponding to both baselines $B = 100$ m and $B = 2$ km. Consequently, the analytical expressions for

the optimal parameters do not apply to the proposed number of pulses and their corresponding pulse efficiencies, given the spatial constraints imposed by the baseline.

V. NUMERICAL OPTIMIZATION

To incorporate the spatial restrictions imposed by the baseline, we transition from the analytical optimization to numerical methods. Relying on numerics, we loosen some of the assumptions made in the analytical optimization above. Instead of treating the number of diamonds and LMT pulses as continuous parameters, we restrict them to integer values. Furthermore, the number of LMT pulses is not fixed but bounded from above by the total number of pulses according to $N < 0.5 + (N_P - 1)/(4Q)$, where $N_P \approx 1.6 \times 10^5$ is derived from the proposed value $N = 4 \times 10^4$ for a single diamond. The same holds for the interferometer time, which does not have to equal the fountain time but is only limited by it from above. In contrast to the analytical optimization, the numerical optimization checks whether an atom interferometer reaches the lower or upper end of the baseline. Moreover, instead of considering the height of the midpoint trajec-

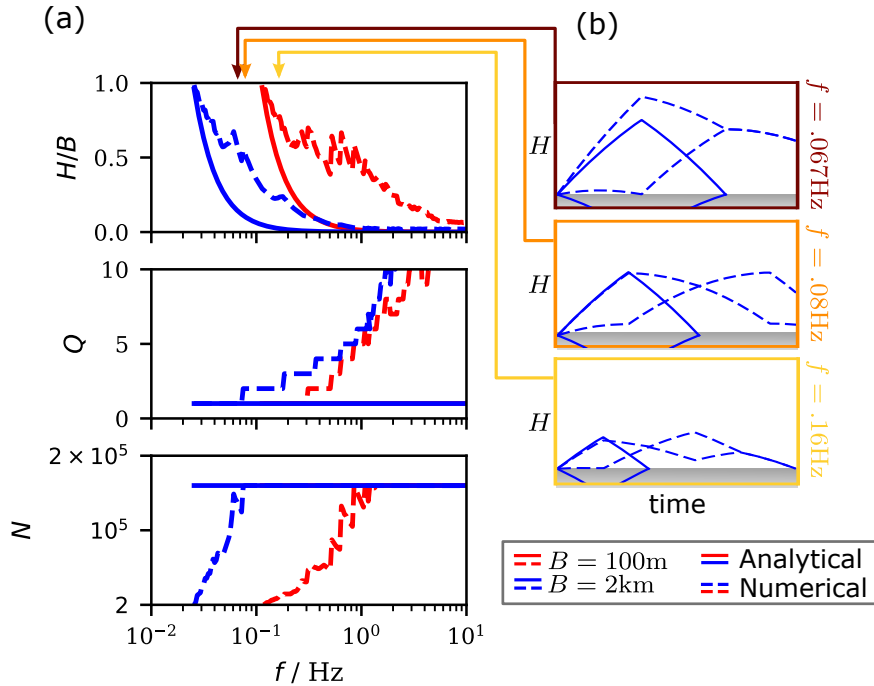


Figure 3. (a) Comparison of the optimal normalized fountain height $\ell = H/B$, number of diamonds Q , and LMT pulses N , shown both with (dashed lines) and without (solid lines) accounting for arm separation as a function of the gravitational wave frequency f for two different baselines B (red and blue). The analytical relations for the optimal parameters neglecting the arm separation are provided in appendix A. In contrast to the analytical optimization, the number of LMT pulses is constrained by the total number of pulses [11] $N_P \approx 1.6 \times 10^5$, while the total interferometer time is limited by the fountain time. (b) Visualization of optimal configurations for three different frequencies to illustrate the influence of arm separation on the optimization.

tory as in the analytical optimization, we determine the actual height of a single atom interferometer and optimize the sensitivity from equation (1) without applying the approximation $\omega\tau_B N \ll 1$.

The relative fountain height, number of diamonds, and LMT pulses for optimal configurations depending on the frequency, both considering and neglecting arm separation, are compared in figure 3 for both baselines $B = 100$ m and $B = 2$ km. Taking arm separation and baseline restrictions into account leads to larger relative heights and an increased number of diamonds with an increasing frequency. In addition, peaks in the relative height arise because the optimal configuration no longer utilizes the entire fountain time. As a consequence, the trajectory appears to bounce off the bottom of the baseline since the optimization simultaneously maximizes the number of LMT pulses while minimizing the relative height, as illustrated in figure 3(b).

The effect of the top of the baseline can be observed in the number of LMT-pulses. Up to a critical frequency, the number of LMT pulses remains constant. However, below this frequency it decreases, because at low frequencies the upper arm of the interferometer reaches the top of the baseline. To remain in resonant mode, the arm separation

is decreased by reducing the number of LMT pulses. This behavior is described by equation (6) and visualized by the blue shaded regions in figure 2(b). There exists a minimal frequency below which the resonant-mode condition cannot be satisfied. This critical frequency is higher for shorter baselines. To probe frequencies below this limit, it is necessary to switch to broadband mode.

In the regime of interest, we observe arm separations on the order of $H \approx 0.5B$, which corresponds to a km-scale for a baseline of $B = 2$ km. This is several orders of magnitude larger than the arm separations achieved experimentally, which have reached up to half a meter [63]. In addition, the total interferometer time $T_{AI} = 2QT$ reaches approximately 5 s for a baseline of $B = 100$ m and exceeds 10 s for $B = 2$ km. To observe interference at the detectors, coherence times longer than $T_{AI} \approx 10$ s are necessary. Furthermore, to optimally utilize $N_P \approx 1.6 \times 10^5$, losses per pulse of $\lambda \approx 1.25 \times 10^{-5}$ are required, as estimated by equation (5). This efficiency target is two orders of magnitude better than the current state-of-the-art losses per pulse of around [56] $\lambda = 1.1 \times 10^{-3}$. Achieving these ambitious pulse efficiencies demands significant advances in pulse fidelity, coherence time, and collimation of the atomic cloud [64–66].

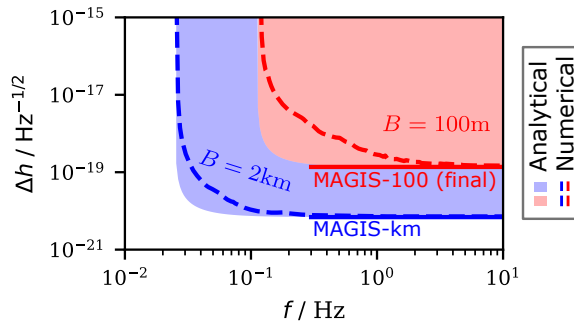


Figure 4. Comparison of the optimal achievable strain uncertainty Δh for two different baselines as a function of gravitational wave frequency. The shaded regions represent the achievable sensitivity neglecting the arm separation, whereas the dashed lines explicitly take it into account. Optimal parameters are visualized in figure 3, and analytical relations neglecting the arm separation are provided in appendix A. In contrast to the analytical optimization, the number of LMT pulses is constrained by the total number of pulses [11] $N_P \approx 1.6 \times 10^5$, while the total interferometer time is limited by the fountain time. The solid lines represent the sensitivities targeted by the MAGIS project [11] above 0.3 Hz, rescaled to two atomic sources to match the optimization.

The optimal parameters are visualized in figure 3, and analytical relations for the case neglecting arm separation are provided in appendix A. In contrast to the analytical optimization, numerical methods are used to incorporate arm separation as well as upper bounds on the number of large-momentum-transfer (LMT) pulses and the total interferometer duration.

After analyzing the parameters of optimal configurations that respect the arm separations of a single interferometer, we now discuss the effects on the optimized strain uncertainty. To calculate the sensitivity, we take the phase uncertainty $\Delta\Phi = 10^{-5} \text{ Hz}^{-1/2}$ for both baselines, which is commonly assumed in recent proposals [11]. Figure 4 compares the sensitivities obtained with and without accounting for arm separation within the optimization. For comparison, the sensitivities assumed from the MAGIS proposal [11] are rescaled to two atomic sources to match the optimization in this work, visualized as dotted lines in figure 4. At high frequencies, our results recover the projected sensitivities, whereas at lower frequencies, significant deviations are observed. In the low-frequency band of the targeted regime, the arm separation becomes a crucial limiting factor. As the top of the baseline constrains the spatial extent of the interferometer arms, the number of LMT pulses must decrease, leading to a significant reduction in sensitivity.

In the following, we assume the relative losses per pulse of $\lambda_R = 1.1 \times 10^{-3}$ corresponding to the current state of the art [56]. Using equation (5), the optimal number of pulses can be estimated, where the term linear in λ scaling with $\xi^2 \propto Bf^2$ becomes relevant. At frequencies $f < 1 \text{ Hz}$ and pulse-per-pulse atom loss λ_R , the optimal total number of pulses is approximately $N_P \approx 1800$ for both baselines $B = 100 \text{ m}$ and $B = 2 \text{ km}$. However, for the larger baseline of 2 km and higher frequencies, the linear term becomes crucial, reducing the optimal pulse number

to about $N_P \approx 1640$ at frequencies around $f \approx 10 \text{ Hz}$. Nevertheless, the total number of pulses is much smaller than assumed in the MAGIS proposal [11] and used for the optimization above. Consulting figure 2(b), the relative loss λ_R indicated by the dotted gray line shows that the restrictions imposed by the baseline and arm separation are not significant in this regime.

The optimized sensitivities, both including and excluding arm separation, are compared in figure 4. The analytical and numerical optimizations show good agreement, indicating that the effect of arm separation is negligible in the considered parameter regime. Due to the negligible effect of the arm separation, figure 5(a) shows only the parameters obtained from the analytical formulas. In the frequency regime of interest, the relative height is approximately 5% of the baseline, which is significantly smaller than the proposed parameters, as shown in figure 3. Consequently, the arm separation plays a negligible role in the optimization of the multi-diamond geometries. Even though our estimates are less sensitive than targeted by the MAGIS proposal, they remain several orders of magnitude below the value of $5.3 \times 10^{-15} \text{ Hz}^{-1/2}$ assumed for the 100-m baseline, corresponding to a phase uncertainty of $\Delta\phi = 10^{-3} \text{ rad Hz}^{-1/2}$ and state-of-the-art LMT technology with 100 LMT pulses [11].

VI. CONCLUSION

In this article, we have derived the optimal value for the total number of pulses, which depends on the experimental parameters and constraints. It arises from a trade-off between maximizing the number of detected atoms, which is limited by the losses per pulse, and increasing the number of diamonds or LMT pulses to enhance the sensitivity. We have derived analytical relations to estimate optimal

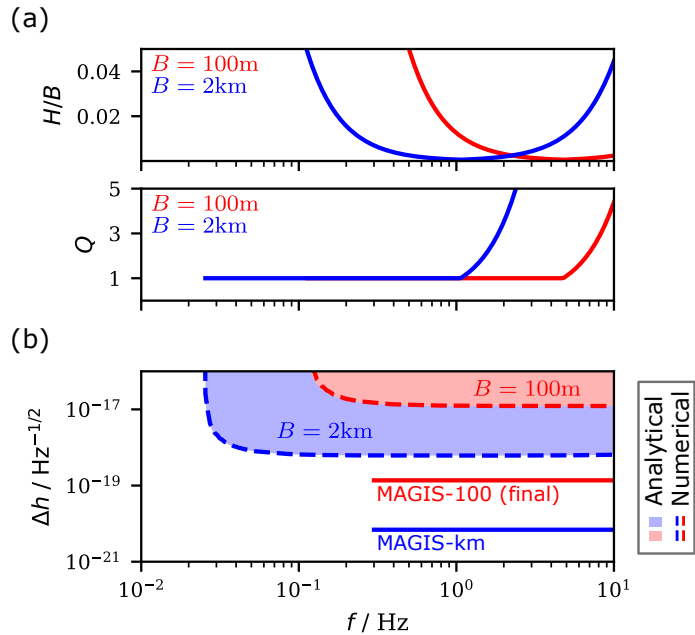


Figure 5. (a) Optimal normalized height $\ell = H/B$ and number of diamonds Q , as well as (b) the corresponding sensitivity for two different baselines as a function of gravitational wave frequency. The number of LMT pulses is constrained by a fixed total number of pulses, estimated using equation (5) for the losses $\lambda_R = 1.1 \times 10^{-3}$ corresponding to the current state of the art [56]. Analytical relations for the case of a fixed total number of pulses are provided in appendix A 2. (b) The shaded regions represent the achievable sensitivity neglecting the arm separation, whereas the dashed lines explicitly take it into account. The solid lines indicate the sensitivities targeted by the MAGIS project [11] above 0.3 Hz, rescaled to two atomic sources to match the optimization. Even though our estimates are less sensitive than the target values, they remain several orders of magnitude below the value of $5.3 \times 10^{-15} Hz^{-1/2}$ assumed for the 100-m baseline, corresponding to a phase uncertainty of $\Delta\phi = 10^{-3} rad Hz^{-1/2}$ and state-of-the-art LMT technology with 100 LMT pulses [11].

pulse numbers for given experimental parameters such as losses per pulse and available baseline. Notably, in the low-frequency band of the targeted regime, the optimal pulse number is primarily determined by atom loss. Small losses allow for large pulse numbers, resulting in greater arm separations, which are fundamentally constrained by the baseline. By explicitly incorporating the spatial limitation imposed by the baseline, we observed a significant reduction in sensitivity in the low-frequency band. So far, neither the losses per pulse nor the arm separation of a single interferometer has been considered in the estimation of proposed sensitivities.

Moreover, pulse imperfections can generate parasitic paths, which reduce sensitivity by in-coupling into the exit port [59–62]. To mitigate these effects, several strategies can be employed, including the design of velocity-selective dichroic mirror pulses [54], tailored design of pulse shapes [55, 56], optimal-control techniques [57], destructive interference of parasitic paths, and coherent enhancement [58].

Another limitation is imposed by the coherence time, expansion duration, temperature, and collimation of the atomic cloud. In optimized configurations, interferometer times can reach 5 s for a baseline of $B \sim 100 m$ and exceed 10 s for $B \sim 2 km$, with corresponding arm separations on

the order of km. These values surpass current state-of-the-art capabilities in both arm separation [63] and expansion duration of the atomic cloud by orders of magnitude. To account for these constraints, it is necessary to impose upper limits on the total atom interferometer duration and arm separation. In addition, this underlines the need for techniques like delta-kick collimation [64–66].

When considering state-of-the-art losses per pulse and the corresponding optimal number of pulses, the arm separation plays a negligible role and does not currently present a limitation. While our estimates do not reach the sensitivities targeted in the MAGIS proposal above 0.3 Hz for a 100-m baseline, our results demonstrate that, with state-of-the-art LMT technology, $N_P = 1800$ LMT pulses can be achieved—an order of magnitude improvement over $N_P = 100$ considered in the initial stage of MAGIS [11]. This indicates that already current technology enables sensitivities better than anticipated by these conservative estimates.

An additional strategy to increase sensitivity is to enhance the signal utilizing entangled atoms [67–69], which enables sensitivities below the shot-noise limit. We expect that the use of entanglement will not directly affect the optimization procedure. However, losses per pulse can rapidly destroy the entanglement, thereby re-

ducing its potential advantage [70]. The compatibility of entanglement-enhanced detection with LMT and multi-diamond schemes in long-baseline setups remains to be verified.

In this work, we have considered the effects of finite speed of light only on the scale of the baseline and between both interferometers. For a large number of LMT pulses, the finite speed of light also becomes relevant on the scale of a single interferometer, resulting in additional phase contributions [71]. These contributions can be minimized by adjusting the resonant condition and by considering time-asymmetric configurations [72].

While our primary focus has been on gravitational-wave detectors, atom interferometers driven by single-photon transitions are also susceptible to ultralight scalar dark matter candidates [10, 73], exhibiting a sensitivity analogous to that for gravitational waves [4, 8, 52]. Therefore, our results can also be applied to the optimization [48] of atom-interferometric dark-matter detectors.

Appendix A: Analytical optimization

1. Case including atom loss

The strain uncertainty obtained by Gaussian error propagation is given by

$$\Delta h = \sqrt{\frac{2}{\nu N_0 (1-\lambda)^{N_P}} \frac{1}{2kLNQ}} \quad (\text{A1})$$

with the initial number of atoms N_0 , the relative losses per pulse λ , and the wave vector k of the laser pulse. The differential measurement scheme employs two interferometers separated by a distance L , with the height H of each interferometer fountain contained within the baseline B . The total number of pulses N_P is related to the number of diamonds Q and the number N of LMT pulses per diffraction sequence through the relation $N_P = 4QN - 2Q + 1$.

Furthermore, we impose two conditions: (i) The interferometer time is chosen as $T_{\text{AI}} = 2QT$, equal to the fountain time $T_{\text{tot}} = \sqrt{8H/g}$. This leads to the relation $Q = \xi\sqrt{\ell}$ with $\xi = \sqrt{2B/(gT^2)}$ and $\ell = H/B$. (ii) We assume the maximal exploitation of the total number of pulses.

Taking these assumptions into account, the strain uncertainty can be written as

$$\Delta h \propto \left[(1-\lambda)^{\frac{N_P-1}{2}} (1-\ell) \left(\xi\sqrt{\ell} + \frac{N_P-1}{2} \right) \right]^{-1}. \quad (\text{A2})$$

We optimize equation (A2) with respect to the relative fountain height ℓ and the total number of pulses N_P . The minimal strain uncertainty is observed for an optimal height

$$\sqrt{\ell} = \frac{1}{\xi \log(1-\lambda)} + \sqrt{\left(\frac{1}{\xi \log(1-\lambda)} \right)^2 + 1} \quad (\text{A3})$$

and an optimal total number of pulses

$$N_P = \frac{-4}{\log(1-\lambda)} - 2\sqrt{\left(\frac{1}{\log(1-\lambda)} \right)^2 + \xi^2 + 1}, \quad (\text{A4})$$

reducing to $N_P \approx \frac{2}{\lambda} + (-1/6 - \xi^2)\lambda$ for small loss $\lambda \ll 1$. Derived from the relative height, the optimal number of diamonds yields

$$Q = \xi\sqrt{\ell} = \frac{1}{\log(1-\lambda)} + \sqrt{\left(\frac{1}{\log(1-\lambda)} \right)^2 + \frac{8B}{g} f^2}. \quad (\text{A5})$$

We observe that for higher frequencies, the number of diamonds increases. Since Q and N are related through the total number of pulses, namely $N_P = 4QN - 2Q + 1$, the number of LMT pulses per diamond decreases. However, at least $N = 2$ is required, defining the high-frequency regime. In contrast, at lower frequencies, the number of diamonds decreases, resulting in a low-frequency regime where the optimal configuration is achieved with the minimal number of diamonds, namely $Q = 1$.

In this low-frequency regime, *i. e.* $Q = 1$, the relative height is described by $\sqrt{\ell} = 1/\xi$, and the total number of pulses takes the form

$$N_P = \frac{-2}{\log(1-\lambda)} - 1 \approx \frac{2}{\lambda}. \quad (\text{A6})$$

In the high-frequency regime, *i. e.* $N = 2$, the total number of pulses can be expressed by $N_P - 1 = 6\xi\sqrt{\ell}$, and the relative height is defined by the nonlinear equation

$$\Delta h \propto \left[4\xi\sqrt{\ell} (1-\lambda)^{3\xi\sqrt{\ell}} (1-\ell) \right]^{-1}. \quad (\text{A7})$$

2. Lossless case

The lossless case $\lambda = 0$ must be considered separately. Because the phase uncertainty no longer depends explicitly on N_P , there is no well-defined optimal number of pulses. Therefore, we assume a fixed N_P and optimize solely with respect to the relative height ℓ . The strain uncertainty in the lossless case then takes the form

$$\Delta h \propto \left[(1-\ell) \left(\xi\sqrt{\ell} + \frac{N_P-1}{2} \right) \right]^{-1} \quad (\text{A8})$$

and the optimal relative height is given by

$$\sqrt{\ell} = \sqrt{\frac{1}{3} + \left(\frac{N_P-1}{6\xi} \right)^2} - \frac{N_P-1}{6\xi}. \quad (\text{A9})$$

ACKNOWLEDGEMENTS

We thank O. Buchmüller, C. McCabe, F. Di Pumpo, A. Friedrich, and T. Kovachy for stimulating discussions

and suggestions. We acknowledge contributions from the Terrestrial Very-Long-Baseline Atom Interferometry (TVLBAI) proto-collaboration. The QUANTUS-VI project is supported by the German Space Agency at the German Aerospace Center (Deutsche Raumfahrtagentur im Deutschen Zentrum für Luft- und Raumfahrt, DLR) with funds provided by the Federal Ministry for Economic Affairs and Climate Action (Bundesministerium für Wirtschaft und Klimaschutz, BMWK) due to an enactment of the German Bundestag under grant no. 50WM2450E (QUANTUS-VI).

COMPETING INTERESTS

The authors declare that they have no competing interests.

DATA AND MATERIALS AVAILABILITY

All data needed to evaluate the conclusions in the paper are present in the paper.

References

- [1] S. Abend *et al.*, Terrestrial very-long-baseline atom interferometry: Workshop summary, *AVS Quantum Sci.* **6**, 024701 (2024).
- [2] A. Abdalla *et al.*, Terrestrial Very-Long-Baseline Atom Interferometry: summary of the second workshop, *EPJ Quantum Technol.* **12**, 42 (2025).
- [3] A. Balaz *et al.*, Long-Baseline Atom Interferometry, [arXiv:2503.21366](https://arxiv.org/abs/2503.21366) (2025).
- [4] S. Dimopoulos, P. W. Graham, J. M. Hogan, M. A. Kasevich, and S. Rajendran, Atomic gravitational wave interferometric sensor, *Phys. Rev. D* **78**, 122002 (2008).
- [5] J. M. Hogan, D. M. S. Johnson, S. Dickerson, T. Kovachy, A. Sugarbaker, S.-w. Chiow, P. W. Graham, M. A. Kasevich, B. Saif, S. Rajendran, P. Bouyer, B. D. Seery, L. Feinberg, and R. Keski-Kuha, An atomic gravitational wave interferometric sensor in low earth orbit (AGIS-LEO), *Gen. Relativ. Gravit.* **43**, 1953 (2011).
- [6] P. W. Graham, J. M. Hogan, M. A. Kasevich, and S. Rajendran, New Method for Gravitational Wave Detection with Atomic Sensors, *Phys. Rev. Lett.* **110**, 171102 (2013).
- [7] P. W. Graham, J. M. Hogan, M. A. Kasevich, and S. Rajendran, Resonant mode for gravitational wave detectors based on atom interferometry, *Phys. Rev. D* **94**, 104022 (2016).
- [8] A. Arvanitaki, P. W. Graham, J. M. Hogan, S. Rajendran, and K. Van Tilburg, Search for light scalar dark matter with atomic gravitational wave detectors, *Phys. Rev. D* **97**, 075020 (2018).
- [9] L. Badurina, D. Blas, and C. McCabe, Refined ultralight scalar dark matter searches with compact atom gradiometers, *Phys. Rev. D* **105**, 023006 (2022).
- [10] D. Derr and E. Giese, Clock transitions versus Bragg diffraction in atom-interferometric dark-matter detection, *AVS Quantum Sci.* **5**, 044404 (2023).
- [11] M. Abe *et al.*, Matter-wave Atomic Gradiometer Interferometric Sensor (MAGIS-100), *Quantum Sci. Technol.* **6**, 044003 (2021).
- [12] L. Badurina *et al.*, AION: an atom interferometer observatory and network, *J. Cosmol. Astropart. Phys.* **2020**, 011.
- [13] B. Canuel *et al.*, ELGAR—a European Laboratory for Gravitation and Atom-interferometric Research, *Class. Quantum Grav.* **37**, 225017 (2020).
- [14] M.-S. Zhan *et al.*, ZAIGA: Zhaoshan long-baseline atom interferometer gravitation antenna, *Int. J. Mod. Phys. D* **29**, 1940005 (2020).
- [15] B. Canuel *et al.*, Exploring gravity with the MIGA large scale atom interferometer, *Sci. Rep.* **8**, 14064 (2018).
- [16] J. Harms, Terrestrial Gravity Fluctuations, *Living Rev. Relativ.* **18**, 3 (2015).
- [17] J. Carlton and C. McCabe, Mitigating anthropogenic and synanthropic noise in atom interferometer searches for ultralight dark matter, *Phys. Rev. D* **108**, 123004 (2023).
- [18] J. Carlton, V. Gibson, T. Kovachy, C. McCabe, and J. Mitchell, Characterizing atmospheric gravity gradient noise for vertical atom interferometers, *Phys. Rev. D* **111**, 082003 (2025).
- [19] P. R. Saulson, Terrestrial gravitational noise on a gravitational wave antenna, *Phys. Rev. D* **30**, 732 (1984).
- [20] B. Canuel *et al.*, Technologies for the elgar large scale atom interferometer array, [arXiv:2007.04014](https://arxiv.org/abs/2007.04014) (2020).
- [21] W. Chaibi, R. Geiger, B. Canuel, A. Bertoldi, A. Landragin, and P. Bouyer, Low frequency gravitational wave detection with ground-based atom interferometer arrays, *Phys. Rev. D* **93**, 021101 (2016).
- [22] L. Badurina, V. Gibson, C. McCabe, and J. Mitchell, Ultralight dark matter searches at the sub-hz frontier with atom multigradiometry, *Phys. Rev. D* **107**, 055002 (2023).
- [23] J. Le Gouët, P. Cheinet, J. Kim, D. Holleville, A. Clairon, A. Landragin, and F. Pereira Dos Santos, Influence of lasers propagation delay on the sensitivity of atom interferometers, *Eur. Phys. J. D* **44**, 419 (2007).
- [24] S. Böhringer, F. Kienle, and R. Lopp, Evolution of momentum-dependent observables under stochastic phase noise in Rabi oscillations, *Phys. Rev. Res.* **7**, 023048 (2025).
- [25] L. Hu, N. Poli, L. Salvi, and G. M. Tino, Atom Interferometry with the Sr Optical Clock Transition, *Phys. Rev. Lett.* **119**, 263601 (2017).
- [26] L. Hu, E. Wang, L. Salvi, J. N. Tinsley, G. M. Tino, and N. Poli, Sr atom interferometry with the optical clock transition as a gravimeter and a gravity gradiometer, *Class. Quantum Grav.* **37**, 014001 (2019).
- [27] J. Rudolph, T. Wilkason, M. Nantel, H. Swan, C. M. Holland, Y. Jiang, B. E. Garber, S. P. Carman, and J. M. Hogan, Large Momentum Transfer Clock Atom Interferometry on the 689 nm Intercombination Line of Strontium, *Phys. Rev. Lett.* **124**, 083604 (2020).
- [28] A. Bott, F. Di Pumpo, and E. Giese, Atomic diffraction from single-photon transitions in gravity and Standard-Model extensions, *AVS Quantum Sci.* **5**, 044402 (2023).
- [29] P. Cladé, S. Guellati-Khélifa, F. Nez, and F. Biraben, Large Momentum Beam Splitter Using Bloch Oscillations, *Phys. Rev. Lett.* **102**, 240402 (2009).
- [30] G. D. McDonald, C. C. N. Kuhn, S. Bennetts, J. E. Debs, K. S. Hardman, M. Johnsson, J. D. Close, and N. P. Robins, $\hbar k$ momentum separa-

- tion with Bloch oscillations in an optically guided atom interferometer, *Phys. Rev. A* **88**, 053620 (2013).
- [31] Z. Pagel, W. Zhong, R. H. Parker, C. T. Olund, N. Y. Yao, and H. Müller, Symmetric Bloch oscillations of matter waves, *Phys. Rev. A* **102**, 053312 (2020).
- [32] T. Rahman, A. Wirth-Singh, A. Ivanov, D. Gochnauer, E. Hough, and S. Gupta, Bloch oscillation phases investigated by multipath Stückelberg atom interferometry, *Phys. Rev. Res.* **6**, L022012 (2024).
- [33] F. Fitzek, J.-N. Kirsten-Siemß, E. M. Rasel, N. Gaaloul, and K. Hammerer, Accurate and efficient Bloch-oscillation-enhanced atom interferometry, *Phys. Rev. Res.* **6**, L032028 (2024).
- [34] T. Lévêque, A. Gauguet, F. Michaud, F. Pereira Dos Santos, and A. Landragin, Enhancing the Area of a Raman Atom Interferometer Using a Versatile Double-Diffraction Technique, *Phys. Rev. Lett.* **103**, 080405 (2009).
- [35] E. Giese, A. Roura, G. Tackmann, E. M. Rasel, and W. P. Schleich, Double Bragg diffraction: A tool for atom optics, *Phys. Rev. A* **88**, 053608 (2013).
- [36] J. Küber, F. Schmaltz, and G. Birkl, Experimental realization of double Bragg diffraction: robust beamsplitters, mirrors, and interferometers for Bose-Einstein condensates, [arXiv:1603.08826](https://arxiv.org/abs/1603.08826) (2016).
- [37] S. Hartmann, J. Jenewein, E. Giese, S. Abend, A. Roura, E. M. Rasel, and W. P. Schleich, Regimes of atomic diffraction: Raman versus Bragg diffraction in retroreflective geometries, *Phys. Rev. A* **101**, 053610 (2020).
- [38] H. Müller, S. Chiow, Q. Long, S. Herrmann, and S. Chu, Atom Interferometry with up to 24-Photon-Momentum-Transfer Beam Splitters, *Phys. Rev. Lett.* **100**, 180405 (2008).
- [39] P. Berg, S. Abend, G. Tackmann, C. Schubert, E. Giese, W. P. Schleich, F. A. Narducci, W. Ertmer, and E. M. Rasel, Composite-Light-Pulse Technique for High-Precision Atom Interferometry, *Phys. Rev. Lett.* **114**, 063002 (2015).
- [40] J. M. McGuirk, M. J. Snadden, and M. A. Kasevich, Large Area Light-Pulse Atom Interferometry, *Phys. Rev. Lett.* **85**, 4498 (2000).
- [41] J. F. Clauser, Ultra-high sensitivity accelerometers and gyroscopes using neutral atom matter-wave interferometry, *Physica B+C* **151**, 262 (1988).
- [42] K.-P. Marzlin and J. Audretsch, State independence in atom interferometry and insensitivity to acceleration and rotation, *Phys. Rev. A* **53**, 312 (1996).
- [43] S. Kleinert, E. Kajari, A. Roura, and W. P. Schleich, Representation-free description of light-pulse atom interferometry including non-inertial effects, *Phys. Rep.* **605**, 1 (2015).
- [44] F. Di Pumpo, A. Friedrich, C. Ufrecht, and E. Giese, Universality-of-clock-rates test using atom interferometry with T^3 scaling, *Phys. Rev. D* **107**, 064007 (2023).
- [45] C. Schubert, S. Abend, M. Gersemann, M. Gebbe, D. Schlippert, P. Berg, and E. M. Rasel, Multi-loop atomic Sagnac interferometry, *Sci. Rep.* **11**, 16121 (2021).
- [46] S. Abend, M. Gebbe, M. Gersemann, H. Ahlers, H. Müntinga, E. Giese, N. Gaaloul, C. Schubert, C. Lämmerzahl, W. Ertmer, W. P. Schleich, and E. M. Rasel, Atom-Chip Fountain Gravimeter, *Phys. Rev. Lett.* **117**, 203003 (2016).
- [47] C. Schubert, D. Schlippert, M. Gersemann, S. Abend, E. Giese, A. Roura, W. P. Schleich, W. Ertmer, and E. M. Rasel, A scalable, symmetric atom interferometer for infrasound gravitational wave detection, *AVS Quantum Sci.* **6**, 044404 (2024).
- [48] F. Di Pumpo, A. Friedrich, and E. Giese, Optimal baseline exploitation in vertical dark-matter detectors based on atom interferometry, *AVS Quantum Sci.* **6**, 014404 (2024).
- [49] Y. A. El-Neaj *et al.*, AEDGE: Atomic Experiment for Dark Matter and Gravity Exploration in Space, *EPJ Quantum Technol.* **7**, 1 (2020).
- [50] D. Savoie, M. Altorio, B. Fang, L. A. Sidorenkov, R. Geiger, and A. Landragin, Interleaved atom interferometry for high-sensitivity inertial measurements, *Sci. Adv.* **4**, eaau7948 (2018).
- [51] L. Badurina, A. Beniwal, and C. McCabe, Super-Nyquist ultralight dark matter searches with broadband atom gradiometers, *Phys. Rev. D* **108**, 083016 (2023).
- [52] L. Badurina, O. Buchmueller, J. Ellis, M. Lewicki, C. McCabe, and V. Vaskonen, Prospective sensitivities of atom interferometers to gravitational waves and ultralight dark matter, *Philos. Trans. R. Soc. A* **380**, 20210060 (2021).
- [53] M. G. Beker, J. F. J. van den Brand, E. Hennes, and D. S. Rabeling, Newtonian noise and ambient ground motion for gravitational wave detectors, *J. Phys.: Conf. Ser.* **363**, 012004 (2012).
- [54] D. Pfeiffer, M. Dietrich, P. Schach, G. Birkl, and E. Giese, Dichroic mirror pulses for optimized higher-order atomic Bragg diffraction, *Phys. Rev. Res.* **7**, L012028 (2025).
- [55] T. Wilkason, M. Nantel, J. Rudolph, Y. Jiang, B. E. Garber, H. Swan, S. P. Carman, M. Abe, and J. M. Hogan, Atom Interferometry with Floquet Atom Optics, *Phys. Rev. Lett.* **129**, 183202 (2022).
- [56] T. Rodzinka, E. Dionis, L. Calmels, S. Beldjoudi, A. Béguin, D. Guéry-Odelin, B. Allard, D. Sugny, and A. Gauguet, Optimal Floquet state engineering for large scale atom interferometers, *Nat. Commun.* **15**, 10281 (2024).
- [57] Y. Wang, J. Glick, T. Deshpande, K. DeRose, S. Saraf, N. Sachdeva, K. Jiang, Z. Chen, and T. Kovachy, Robust Quantum Control via Multipath Interference for Thousandfold Phase Amplification in a Resonant Atom Interferometer, *Phys. Rev. Lett.* **133**, 243403 (2024).
- [58] A. Béguin, T. Rodzinka, L. Calmels, B. Allard, and A. Gauguet, Atom Interferometry with Coherent Enhancement of Bragg Pulse Sequences, *Phys. Rev. Lett.* **131**, 143401 (2023).
- [59] A. Béguin, T. Rodzinka, J. Vigué, B. Allard, and A. Gauguet, Characterization of an atom interferometer in the quasi-Bragg regime, *Phys. Rev. A* **105**, 033302 (2022).
- [60] P. A. Altin, M. T. Johnsson, V. Negnevitsky, G. R. Dennis, R. P. Anderson, J. E. Debs, S. S. Szigeti, K. S. Hardman, S. Bennetts, G. D. McDonald, L. D. Turner, J. D. Close, and N. P. Robins, Precision atomic gravimeter based on Bragg diffraction, *New J. Phys.* **15**, 023009 (2013).
- [61] R. H. Parker, C. Yu, B. Estey, W. Zhong, E. Huang, and H. Müller, Controlling the multiport nature of Bragg diffraction in atom interferometry, *Phys. Rev. A* **94**, 053618 (2016).
- [62] J. Jenewein, S. Hartmann, A. Roura, and E. Giese, Bragg-diffraction-induced imperfections of the signal in retroreflective atom interferometers, *Phys. Rev. A* **105**, 063316 (2022).
- [63] T. Kovachy, P. Asenbaum, C. Overstreet, C. A. Donnelly, S. M. Dickerson, A. Sugarbaker, J. M. Hogan, and M. A. Kasevich, Quantum superposition at the half-metre scale, *Nature* **528**, 530 (2015).

- [64] H. Ammann and N. Christensen, Delta kick cooling: A new method for cooling atoms, *Phys. Rev. Lett.* **78**, 2088 (1997).
- [65] H. Müntinga, H. Ahlers, M. Krutzik, A. Wenzlawski, S. Arnold, D. Becker, K. Bongs, H. Dittus, H. Duncker, N. Gaaloul, C. Gherasim, E. Giese, C. Grzeschik, T. W. Hänsch, O. Hellmig, W. Herr, S. Herrmann, E. Kajari, S. Kleinert, C. Lämmerzahl, W. Lewoczko-Adamczyk, J. Malcolm, N. Meyer, R. Nolte, A. Peters, M. Popp, J. Reichel, A. Roura, J. Rudolph, M. Schiemangk, M. Schneider, S. T. Seidel, K. Sengstock, V. Tamma, T. Valenzuela, A. Vogel, R. Walser, T. Wendrich, P. Windpassinger, W. Zeller, T. van Zoest, W. Ertmer, W. P. Schleich, and E. M. Rasel, Interferometry with bose-einstein condensates in microgravity, *Phys. Rev. Lett.* **110**, 093602 (2013).
- [66] T. Kovachy, J. M. Hogan, A. Sugarbaker, S. M. Dickerson, C. A. Donnelly, C. Overstreet, and M. A. Kasevich, Matter wave lensing to picokelvin temperatures, *Phys. Rev. Lett.* **114**, 143004 (2015).
- [67] O. Hosten, N. J. Engelsen, R. Krishnakumar, and M. A. Kasevich, Measurement noise 100 times lower than the quantum-projection limit using entangled atoms, *Nature* **529**, 505 (2016).
- [68] F. Anders, A. Idel, P. Feldmann, D. Bondarenko, S. Lori-ani, K. Lange, J. Peise, M. Gersemann, B. Meyer-Hoppe, S. Abend, N. Gaaloul, C. Schubert, D. Schlippert, L. Santos, E. Rasel, and C. Klempt, Momentum Entanglement for Atom Interferometry, *Phys. Rev. Lett.* **127**, 140402 (2021).
- [69] C. Cassens, B. Meyer-Hoppe, E. Rasel, and C. Klempt, Entanglement-Enhanced Atomic Gravimeter, *Phys. Rev. X* **15**, 011029 (2025).
- [70] J. Günther, J.-N. Kirsten-Siemß, N. Gaaloul, and K. Hammerer, Squeezing Enhancement in Lossy Multi-Path Atom Interferometers, [arXiv:2409.04091](https://arxiv.org/abs/2409.04091) (2024).
- [71] C. Niehof, D. Derr, and E. Giese, Finite-Speed-of-Light Effects in Atom Interferometry: Diffraction Mechanisms and Resonance Conditions, [arXiv:2505.02728](https://arxiv.org/abs/2505.02728) (2025).
- [72] Y.-J. Tan, C.-G. Shao, and Z.-K. Hu, Time delay and the effect of the finite speed of light in atom gravimeters, *Phys. Rev. A* **96**, 023604 (2017).
- [73] F. Di Pumpo, A. Friedrich, A. Geyer, C. Ufrecht, and E. Giese, Light propagation and atom interferometry in gravity and dilaton fields, *Phys. Rev. D* **105**, 084065 (2022).